Rapid and nondestructive prediction of firmness, soluble solids content, and pH in kiwifruit using Vis–NIR spatially resolved spectroscopy

---

Te Ma[a,1], Jian Zhao[a,b,1], Tetsuya Inagaki[a], Yuan Su [a,c], and Satoru Tsuchikawa[a,*]

[a]Graduate School of Bioagricultural Sciences, Nagoya University, Furo-Cho, Chikusa, Nagoya 464-8601, Japan

[b]College of Mechanical and Electronic Engineering, Northwest A&F University, Yangling, Shaanxi 712100, China

[c]College of Engineering, China Agricultural University, NO. 17 Qinghua East Road, Beijing 100083, PR China

***** Corresponding author

Email address: st3842@agr.nagoya-u.ac.jp

Tel/Fax: (+81)527894157

[1] These authors equally contributed to this work.

Te Ma: mate@agr.nagoya-u.ac.jp

Jian Zhao: 2017052634@nwsuaf.edu.cn

Tetsuya Inagaki: inatetsu@agr.nagoya-u.ac.jp

Yuan Su: suyuan0223@cau.edu.cn

CRediT author statement:

The first two authors, Te Ma and Jian Zhao contributed equally to this study (co-first author)

Te Ma: Methodology, Data curation, Validation, Writing-Original draft preparation

Jian Zhao: Methodology, Data curation, Validation, Writing-Original draft preparation

Tetsuya Inagaki: Methodology, Writing-reviewing, and editing

Yuan Su: Data curation, Writing-reviewing, and editing

Satoru Tsuchikawa*: Supervision, Conceptualization, Writing-reviewing, and editing

Abstract

This paper reports an evaluation of firmness, soluble solids content (SSC), and acidity (pH) in kiwifruit using a newly designed visible–near-infrared (Vis–NIR) spatially resolved spectroscopic (SRS) system. The system mainly comprises a cost-effective Vis–NIR hyperspectral imaging camera, a halogen light source, and 36 light-receiving silica fibers which were divided into six groups (1, 2, 3, 4, 5, and 10 mm away from the light illumination) used to collect diffusely reflected light from sample surface. During the experiment, time-resolved spectroscopy (TRS) was used to validate the light scattering characteristics at a single wavelength of 846 nm by transmission measurement, which differed from the reflectance measurement of the SRS system. The TRS results show that firmer kiwifruits tended to have a lower transmitted light intensity and a higher full width at half maximum value. The SRS results indicate that the reflected light intensity decreased more with an increased distance from the illumination spot in firmer kiwifruits. The results of the two methods supported the same view, i.e., firmer kiwifruit indicated higher degrees of light scattering inside. Following on, the calibration models for kiwifruit properties were constructed using the SRS data coupled with partial least squares regression analysis. Finally, the prediction accuracies were benchmarked against standard diffuse reflectance spectroscopy using one fiber group position of the same SRS system. The overall results showed the benefits of using the SRS system to predict fruit firmness by enhancing light scattering effects and predicting the SSC required for reducing such effects.

Keywords: Kiwifruit; nondestructive prediction of firmness, soluble solids content (SSC) and pH; time and spatially resolved spectroscopy; light absorption and scattering; partial least squares (PLS) regression analysis; finite element method.

1. Introduction

Kiwifruit has become a global agricultural commodity because of its unique flavor and health benefits for the digestive system (Guo et al., 2016; Li et al., 2015; Moughan et al., 2013). To ensure its longest possible storage and transport life, kiwifruit is generally harvested pre-climacteric when fruit softening has not yet commenced (Asiche et al., 2017). After being harvested, as a climacteric fruit, the kiwifruit's ripening-associated events continue to develop (Antunes et al., 2000). Generally, there is some variation in the degree of climacteric ripening of fruit (e.g., decay of firmness, sugar accumulation, and color change) during the storage and the transport periods; however, because such ripening variation has not yet been evaluated and sorted in the market, consumers generally tend to choose which kiwifruits to buy by applying light pressure to the fruit with their fingers. Hence, the measurement of firmness, sugar and acid (pH) accumulation is essential not only for suitable postharvest storage and reducing waste but also to satisfy customers and promote sales (Asiche et al., 2017; Goldberg et al., 2019). However, conventional measurement methods, such as Magness–Taylor (MT) firmness testing (Shmulevich et al., 2003) and Brix refractometry (Magwaza and Opara, 2015), are time-consuming and can damage the fruit (Cen et al., 2012). Accordingly, nondestructive, rapid, and easy-to-operate evaluation methods are highly desired.

Visible and near-infrared (Vis–NIR) spectroscopy, primarily combined with multivariate mathematical techniques, is suitable for characterizing the organic compounds present in the fruit (Huang et al., 2014; Nicolaï et al., 2007). Such methods have been well-studied in kiwifruit quality assessment, mainly in the estimation of soluble solids content (SSC) and acidity (Ciccoritti et al., 2019; Fu et al., 2007; Guo et al., 2016; McGlone et al., 2007, 2002; McGlone and Kawano, 1998; Moghimi et al., 2010; Santagapita et al., 2016). Generally,

absorption coefficient (μ_a) and reduced scattering coefficient (μ_s') are used to characterize light propagation in the biological samples, respectively. μ_s' is defined as $\mu_s' = (1-g)\,\mu_s$, where μ_s is scattering coefficient and g is the mean cosine of the scattering angle (Martelli et al., 2009). Since conventional spectrometry can only explain the aggregate effects of light absorption and scattering (Vanoli et al., 2020), most existing studies have chiefly relied on additional spectral pretreatments, such as baseline offset correction or standard normal variate (SNV) transformation (Giovanelli et al., 2014; Rogel-Castillo et al., 2016), to reduce light scattering when determining chemical compounds (Giovanelli et al., 2014; Rogel-Castillo et al., 2016; Zude et al., 2011). However, significant challenges remain in detecting minor chemical changes associated with firmness (McGlone and Kawano, 1998; Walsh et al., 2020).

Although the underlying mechanisms of fruit softening remain unclear, it is generally understood that cell wall modifying enzymes play an essential role in this regard (Brummell and Harpster, 2001); additionally, water-soluble pectin increases during fruit ripening (Chapman and Horvat, 1990). Accordingly, the MT firmness test may be partially dependent on the state of pectin and changes in turgor pressure (Fu et al., 2007). Existing studies found that light scattering characteristics in most agricultural products correlate with their physical structures (Lu et al., 2020; Qin and Lu, 2008), as well as their water content (Ma et al., 2018a; Romano et al., 2011). McGlone et al. (1997) measured diffusely reflected light at 60 mm from the fruit center and several detection angles ranging from 20 to 55° around the circumference of the fruit from incident laser beam direction. Their results showed that as the fruit softened, an increase occurred in the intensity of the diffusely reflected light exiting near the irradiated points. Baranyai and Zude (2009) used a monochromatic light coupled with a camera system for contactless measurement of the diffuse reflectance of kiwifruit, a significant difference ($p < 0.01$) was found between the estimated values of the anisotropy factor of commercial-grade and overripe fruit pieces. Their results suggest that the use of this rich light scattering information is essential for predicting the firmness and ripening process of the fruit rather than reducing it (De Belie et al., 1999; Peng and Lu, 2005; Rizzolo et al., 2014).

Time-resolved spectroscopy (TRS) and spatially resolved spectroscopy (SRS) are commonly used to evaluate the optical properties inside the fruit. The TRS method generally uses very short (picosecond or femtosecond) light pulses. Its photon time-of-flight distribution inside the sample can be evaluated to obtain light absorption and scattering characteristics, based on the diffusion theory (Torricelli et al., 2013; Tsuchikawa, 2002; Vanoli et al., 2011). A reflectance-type TRS method was used to separate the scattering effects from that of light absorption in kiwifruit and correctly classify the used samples into three groups, achieving performance results of 75 % for firmness, 60 % for sugar content, and 97 % for acidity (Valero et al., 2004). Although the TRS method is expensive and time-consuming, which may not be suitable for measuring intact fruit and vegetable products (Cen and Lu, 2010); it is considered more accurate for measuring optical properties (Lu et al., 2020). Additionally, the TRS spectra acquired for the entire fruit were shown to be very similar to the spectra of the same fruit when peeled (Vanoli et al., 2020). In contrast, the SRS method is less expensive in instrumentation and faster in measurement compared to the TRS method. The SRS method diffusely reflects a light pattern at sample surface, which is collected and used to separate light scattering characteristics from light absorption (Farrell et al., 1992; Huang et al., 2018; Lu et al., 2020; Qin et al., 2009). Presently, there are two main configurations for the SRS system. One of these is an imaging-based SRS system that was evaluated for measuring the spatially resolved diffuse reflectance of fruit and vegetables (Ma et al., 2018a; Peng and Lu, 2008; Qin and Lu, 2008; Zhu et al., 2015). The difficulties of the imaging-based SRS system for practical applications include that the distance between the light source and detector must be carefully considered and adjusted (Cen and Lu, 2010; Lu et al., 2020). Contrastingly, the fiber probe-based SRS system approach is a contact method that is often inconvenient for fast on-line quality assessment requirements (Ma et al., 2018b; Vanoli et al., 2020). However, it has a portable design that is easy to operate on-site (Ma et al., 2021).

Typical strategies for separating light scattering information from the SRS data include numerical methods, such as Monte Carlo simulations (Cen and Lu, 2010; Hjalmarsson and

Thennadil, 2007), as well as approximations, e.g., applying the diffusion theory (Adebayo et al., 2017; Farrell et al., 1992). However, the conventional diffusion theory may present instability when light scattering in samples is not dominant over absorption (Lu et al., 2020; Vanoli et al., 2020; Ziosi et al., 2008). Additionally, the derivation of the diffusion equation from the transport equation must assume the scattering is isotropic. However, the scattering is highly anisotropic in biological materials (Lu et al., 2020). Hielscher et al.(1995) illustrated that the μ_s' derived from conventional diffusion equations is incorrect when source-detector distance is short. Comparatively, if the source-detector distance is long, the effects of sample irregular shape on data collection could be another issue when all fibers are fixed to the inflexible probe (Huang et al., 2017). Hence, different designs of the SRS system must be carefully evaluated for the quality evaluation of horticultural products. Additionally, more accurate methods for measuring optical properties, such as the TRS, should be utilized to validate and improve the SRS results.

This study aimed to demonstrate a nondestructive and rapid SRS method for predicting kiwifruit's firmness, SSC, and pH. The objectives of this study are summarized as follows: (1) compare the light scattering characteristics in the same kiwifruit samples derived by the TRS (transmission measurement) and SRS (reflectance measurement) methods; (2) construct calibration models using the SRS system coupled with partial least squares (PLS) regression analysis; and (3) benchmark the prediction results against standard diffuse reflectance spectroscopy on the basis of the same designed system to quantify the added value of the SRS approach.

2. Materials and Method

2.1 Sample preparation

Measurements on calibrated phantoms were done to assess the performance of the TRS and SRS systems in retrieving the optical properties. intralipid 20 % (sc-215182, Santa Cruz

Biotechnology, Texas, USA) was used as scatterer to prepare reference samples with six concentration levels (0.5, 1, 3, 5, 7, and 9 %, respectively)

A total of 120 golden kiwifruits (*Actinidia chinensis*, imported from New Zealand) at the same commercial maturity stage were collected at a local market. The skin of this species is thin, nearly hairless, and has a relatively flat surface at the stem-calyx axis. The data collection was completed in one week. Before recording the required measurements, the samples were stored under cold conditions (3 – 7 °C and 25 – 50 % humidity). Subsequently, the cold-stored samples were moved to room temperature conditions approximately 12 h before conducting the measurements to reduce spectral data variations caused by the temperature differences. Additionally, the diameter of each sample was measured to correct the optical path effects in the TRS transmission measurements.

2.2 Time-resolved spectroscopic measurements

Figure 1 (a) shows the main components of the TRS system. A beam diameter on the sample of approximately 1.5 mm was performed using a picosecond pulsed laser with a wavelength of 846 nm at a pulse width of 70 ps and a peak power of 151 mW (PLP-10; Hamamatsu Photonics Co., Hamamatsu, Japan). The transmitted photons exiting the sample were collected by a 300-μm-diameter optical fiber (A5760-02; Hamamatsu Photonics Co., Hamamatsu, Japan) placed at approximately 10 mm distance from the sample. The transmitted photons were dispersed with a spectroscope equipped with gratings (C11119-02; Hamamatsu Photonics Co., Hamamatsu, Japan). Finally, the time variation of the transmitted radiation intensity was recorded by a streak camera with a time resolution of 10.3 ps (C5680; Hamamatsu Photonics Co., Hamamatsu, Japan). The instrument response function (IRF) was measured using a couple of neutral density filters with 1 % transmission ratio (A5760-02; Hamamatsu Photonics Co., Hamamatsu, Japan). The full width at half maximum (FWHM) of the IRF was approximately 226.14 ps. The time-resolved profiles (TRP) of the intralipid samples were measured in a 1 cm diam glass cell using a time range of 10 ns, and each

photon count was performed for 60 s. The TRP of the kiwifruit samples were acquired from every 120° along the equator line through the sample's skin.

2.3 Time-resolved profile analysis

A Savitzky–Golay filter (polynomial order, 2; frame length, 25) was first applied to smooth out the measured raw TRP. Then, the coefficients μ_a and μ_s' were calculated by fitting the convolution between the IRF and the modeled time-resolved distribution to the TRP (Ban et al., 2018). Briefly, the number of photons reaching the detector surface per unit area per unit time could be expressed as follows (Martelli et al., 1997):

$$T(\rho, t) = \frac{\exp\left(-\mu_a vt - \frac{\rho^2}{4Dvt}\right)}{2(4\pi Dv)^{3/2} t^{5/2}} \sum_{m=-\infty}^{+\infty} \left[\mathcal{Z}_{1,m} \exp\left(-\frac{\mathcal{Z}_{1,m}{}^2}{4Dvt}\right) - \mathcal{Z}_{2,m} \exp\left(-\frac{\mathcal{Z}_{2,m}{}^2}{4Dvt}\right)\right] \quad (1)$$

$$\mathcal{Z}_{1,m} = s(1-2m) - 4m\mathcal{Z}_e - \mathcal{Z}_0 \quad (2)$$

$$\mathcal{Z}_{2,m} = s(1-2m) - (4m-2)\mathcal{Z}_e + \mathcal{Z}_0 \quad (3)$$

$$\mathcal{Z}_0 = 1/\mu_s' \quad (4)$$

$$\mathcal{Z}_e = 2AD \quad (5)$$

$$D = 1/3\mu_s' \quad (6)$$

In the above expression, ρ is the distance from the light incident center, set as 0 for transmittance measurement. *t* and *s* illustrate time and sample thickness, respectively. *v* is the speed of light in vacuum divided by the sample's index of refraction (n). The n and A were set as 1.34 (Fang et al., 2016), and 2.58 (Martelli et al., 1997), respectively. Seven dipoles (m=0, ± 1, ± 2, ± 3) were used. Because μ_s' was significantly larger than μ_a in the sample material at the light wavelength 846 nm. The fitting range for TRP was from 1 to 10 mm^{-1} for μ_s'; and from 0.001 to 0.01 mm^{-1} for μ_a. The fitting method was trust-region-reflective.

2.4 Spatially resolved spectroscopic measurements

Figure 1 (b) shows the main components of the newly designed Vis–NIR SRS system,

which primarily includes a 5W halogen lamp and an optical fiber (SOG-70S; Sumita Optical Glass, Inc., Saitama, Japan), which was used to bring the light source into the sample's measured position. Then, 36 silica fibers (Vis–NIR type, core diameter: 100 μm, clad: 110 μm; Fiberguide Industries, New Jersey, USA) were used to collect the diffusely reflected light from the sample surface and transfer it into a Vis–NIR hyperspectral imaging (HSI) camera (SPECT-100nir1F; Spectral Application Research Laboratory Co., Ltd., Shizuoka, Japan). The 36 silica fibers were separated into six groups. A fiber connecter was used to order the 36 silica fibers horizontally at the side of the HSI camera. Then, the light beam was dispersed by a spectrometer into spectral components (vertical axis) while preserving spatial information (horizontal axis), and the two-dimensional light signals were collected. The SRS fixator was inserted into the intralipid scatters for spatially resolved profiles (SRP) collection. The SRP of the kiwifruit were collected from the same positions as the measured TRP.

2.5 Spatially resolved profile analysis

The raw spatially resolved spectral image includes both spectral information of the object sample and the spatial information provided by the light-receiving fibers. The sensitive wavelength range of the HSI camera was 600–1100 nm with a wavelength resolution of 4.5 nm. This study achieved an improved signal-to-noise ratio by first averaging the signals collected by each fiber (i.e., 30 pixels on the raw image) and then by averaging every six fibers at the same fiber group. The light reference was measured using an integrating sphere (3P-GPS-060-SF; Labsphere, Inc., North Sutton, USA). Dark values were measured by turning off the light and covering the light collection fibers. Wavelengths under 660 nm and above 1000 nm were found to be noisy and unreliable. Hence, a wavelength range of 660–1000 nm was selected, and its relative reflectance values were calculated using Eq. (7):

$$R_{\lambda,n} = \frac{S_{\lambda,n} - D_{\lambda,n}}{B_{\lambda,n} - D_{\lambda,n}} \quad (7)$$

Where R is the diffuse reflectance value at wavelength λ and pixel n; S and B are the sample and white reference image, respectively; and D is the dark image.

A Savitzky–Golay filter (polynomial order, 2; frame length, 5) was applied for the SRP smoothing. The coefficients μ_a and μ_s' were estimated using an analytical solution of the radiative transfer equation for a continuous spot light beam into a highly scattering turbid medium (Martelli et al., 1997). The diffuse reflectance is described as a function of absorption and scattering properties and the radial distance measured from the center of the beam light as below:

$$R(\rho) = -\frac{1}{4\pi}\sum_{m=-\infty}^{+\infty}\left(z_{3,m}\left(\rho^2 + {z_{3,m}}^2\right)^{-3/2} \times \left\{1 + \left[\frac{\mu_a\left(\rho^2+{z_{3,m}}^2\right)}{D}\right]^{1/2}\right\} \times \exp\left\{-\left[\frac{\mu_a\left(\rho^2+{z_{3,m}}^2\right)}{D}\right]^{1/2}\right\} - z_{4,m}\left(\rho^2 + {z_{4,m}}^2\right)^{-3/2} \times \left\{1 + \left[\frac{\mu_a\left(\rho^2+{z_{4,m}}^2\right)}{D}\right]^{1/2}\right\} \times \exp\left\{-\left[\frac{\mu_a\left(\rho^2+{z_{4,m}}^2\right)}{D}\right]^{1/2}\right\} \quad (8)$$

$$z_{3,m} = -2ms - 4mz_e - z_0 \quad (9)$$

$$z_{4,m} = -2ms - (4m-2)z_e + z_0 \quad (10)$$

Where $R(\rho)$ is the reflectance profile at ρ distance from the light incident center, s is the sample diameter for the $z_{3,m}$ and $z_{4,m}$ calculations. Totally, 11 dipoles (m=0, ±1, ±2, ±3, ±4, ±5) was used. The fitting method was the trust-region-reflective.

For comparison, the SRP were also directly analyzed via a curve fitting method based on exponential decay:

$$R(\rho) = \mathrm{a} \times \exp(-\mathrm{b}(\rho)) + \mathrm{c} \quad (11)$$

Where $R(\rho)$ is the reflectance profile at ρ. The parameter values a, b, and c at each wavelength were evaluated to establish a quantitative relationship with the kiwifruit quality.

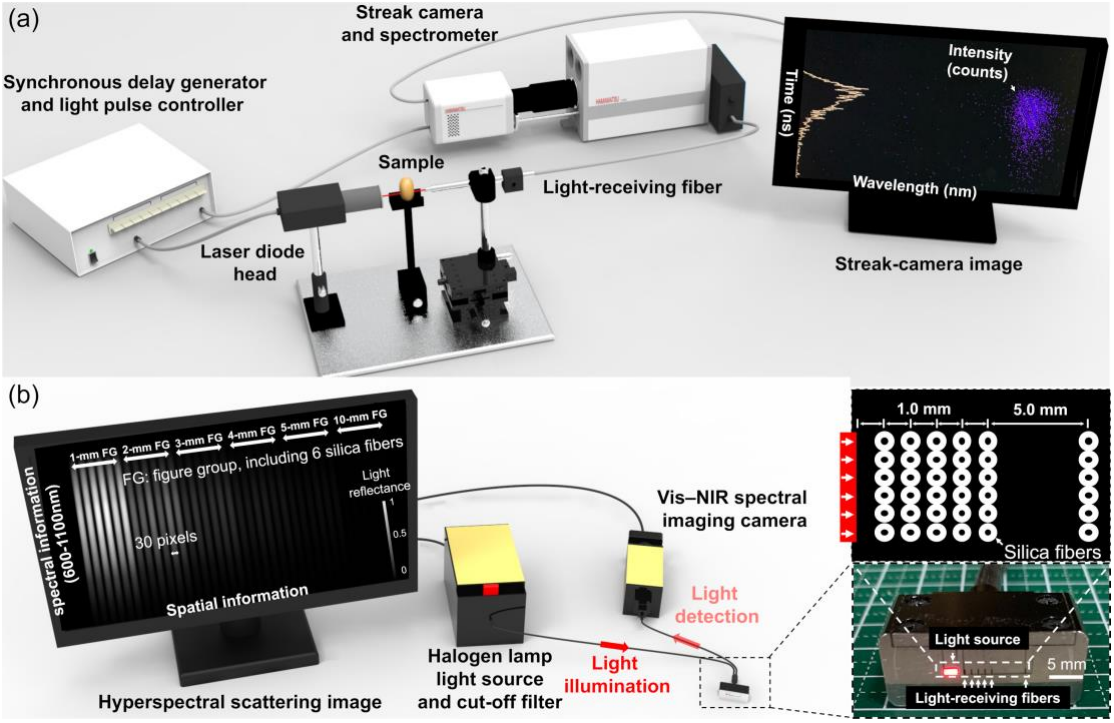

Figure 1. The main components of (a) time- and (b) spatially resolved spectroscopic measurement system.

2.6 Measurement of firmness, soluble solids content, and pH reference values.

The same three positions measured using the TRS and SRS for each sample were firstly measured using a 5-mm-diameter plunger (Fudoh Rheo Meter, Rheotech, Inc., Tokyo, Japan) at a speed of 1mm/s; their resulting mean values were used as sample firmness reference. Then, the fresh juice of each sample was extracted for SSC measurement using a Brix refractometer (IPR-201, Spittz, Atago Co., Ltd., Tokyo, Japan); pH measurements were recorded using a pH meter (LAQUAtwin-pH-22B, Horiba Advanced Techno Co., Ltd., Kyoto, Japan).

2.7 Modeling and simulating the firmness measurements based on the finite element method

Since the targeted golden kiwifruits were at a commercially mature stage, the sarcocarp was much softer compared with fruit that had just been picked. Additionally, this species has a

very thin pericarp; as such, the sample firmness was evaluated via a compression test with the pericarp in this study. To verify the positive correlation between the firmness of the sample sarcocarp and the measured firmness reference values, finite element method (FEM) simulation was adopted to the stress changes of kiwifruit during the compression test. In the simulations, the main consideration was whether the sarcocarp had a significant effect on the firmness of the whole kiwifruit. It was simplified to an isotropic and homogeneously mechanic model. The compression rod was also defined in this way. There was no large deformation or local over deformation of the kiwifruit in the actual pre-compression tests. Hence, the materials meet the assumptions of continuous and small deformations. The mechanical properties (i.e., the densities, elastic moduli, and Poisson's ratios) of the pericarp and sarcocarp were fundamental to the simulation. An electronic scale and an electronic Vernier caliper were used to record the sample masses and measurements. The Poisson's ratios were assumed to be 0.3 based on relevant references (Zhao et al., 2021, 2019). An electronic universal testing machine (Shimadzu AG-100KNI, Shimadzu, Japan) was used to perform physical tests. The sarcocarp was shaped into a cylinder with a height of 20 mm, and the pericarp was made into a cuboid shape with a width of 20 mm and a thickness of 1 mm. The compression test was applied for the sarcocarps of selected samples, and the tensile test was conducted for their pericarps. Additionally, 5 mm/min was selected as the speed of the compression test, and 2 mm/min was selected as the speed of the tensile test. The test results were applied as the mechanical properties in the simulation. The elastic moduli were directly obtained from the stress–strain curves. The stresses and strains were calculated based on the following two equations:

$$\sigma = \frac{F}{A_0} \quad (12)$$

$$\varepsilon = \frac{\Delta l}{l_0} \quad (13)$$

where σ is the stress of the sample, F is the load of test, A_0 is the cross-sectional area, ε is the strain of the sample, Δl is the length change of the sample, and l_0 is the distance between two contact points.

The elastic modulus was determined using the following equation:

$$E = \frac{\sigma}{\varepsilon} \quad (14)$$

where E is the elastic modulus of the sample (MPa).

All simulations based on FEM were performed using the Abaqus software (Dassault Systemes, Vélizy-Villacoublay, France). The three-dimensional (3D) models of pericarp, sarcocarp, and the compression rod were constructed and assembled in the CATIA software (Dassault Systemes, Vélizy-Villacoublay, France). The mechanical properties of the materials (Table 1) were imported into the property module. Then, the parts were assembled in the Assembly module and the simulation time was set to 3.2 s in the Step module. The contact of the two surfaces was defined in the interaction module. The gravitational acceleration was applied to the 3D model in the load module and the model was not subjected to external forces in the initial state. Additionally, because the speed for the firmness reference measurement was 1 mm/s, so the same speed was set in the simulations. For better display, the side of the kiwifruit was cut vertically so that the pericarp and sarcocarp could be viewed clearly.

Table 1. The mechanical properties of materials.

Item	Density (t/mm^3)	Elastic modulus (MPa)	Poisson's ratio
Sarcocarp	1.08E – 9	0.09 and 0.86	0.30
Pericarp	6.58E – 10	3.39	0.30
Compression rod	7.85E + 3	200000	0.25

2.8 Construction of the calibration models by partial least squares regression analysis

PLS regression combines the features of principal component analysis and multiple regression. This method is particularly useful when dependent variables need to be predicted from a large set of independent variables (Martens and Tormod, 1992; Yang et al., 2017). During the PLS regression model development, a subset comprising 80 % of all the 120 kiwifruits included in the study was randomly selected as a calibration set, leaving 20 % for inclusion in a validation set. The coefficients of determination (R^2) and the root mean square

error (RMSE) of five-fold cross-validation was used to optimize the best number of latent variants (LVs) as shown below:

$$R^2 = 1 - \frac{\sum_{i=1}^{n}(y_i - \hat{y}_i)^2}{\sum_{i=1}^{n}(y_i - \bar{y})^2} \quad (15)$$

$$\mathrm{RMSE} = \sqrt{\frac{1}{n}\sum_{i=1}^{n}(\hat{y}_i - y_i)^2} \quad (16)$$

where n is the number of samples, y is the reference value, $\hat{y}$ is the value predicted by NIR spectroscopy, and $\bar{y}$ is the mean values of y.

A competitive adaptive reweighed sampling (CARS) method was used for wavelength selection. Briefly, the CARS could select N subsets of explanatory variables (EVs) via Monte Carlo runs. Their PLS regression coefficients were compared for ranking the contribution of each EV. The purpose of doing so was to reduce the number of EVs against overfitting. More details of this technique can be found in Li et al. (2009). The Matlab R2020a (The MathWorks Inc., Natick, MA, USA) was used for conducting image processing and data analysis procedures.

3. Results and discussion

Figure 2 (a_1) shows the TRP at wavelength 846 nm, illustrating the calibrated phantoms with higher light scattering tended to have a lower transmitted light intensity and longer transmission time, i.e., a higher FWHM value. Due to overexposure, the lowest intralipid concentration level at 0.5 % is not shown. Figure 2 (b_1) shows the SRP at the same wavelength 846 nm, indicating the calibrated phantoms with higher light scattering tended to decrease significantly with an increased distance from the illumination spot. Figure 2 (a_2) and (b_2) show the estimated μ_s' values by the TRS and the SRS, respectively. The μ_s' (TRS) values were in good agreement with previous studies (Aernouts et al., 2013; Sun et al., 2021), suggesting the variation in scattering was linked well with the TRP. Compared with the results in the literature (Huang et al., 2017; Michels et al., 2008), this study showed a highly nonlinear relationship between the estimated μ_s' (SRS) values and the intralipid contents. This

suggests the designed SRS system requires further improvements to better meet the diffusion equation's requirements, especially to estimate a wide range of the μ_s' (SRS). The size of the light illumination spot was enlarged in this study (Figure 1 (b)), which could cause a flatter decreasing trend with the increasing distance from the illumination center. Additionally, the source-detector distance was short; photos may not have lost their initial directionality (i.e., could not be considered as diffuse). However, suppose the size of the illumination spot is reduced and the source-detector distance is increased; in that case, a lower signal-to-noise ratio and the effects caused by the irregular shape of the kiwifruit could be another issue. The utilization of optimization algorithms for further correct the estimated μ_s' (SRS) is beyond the scope of this article.

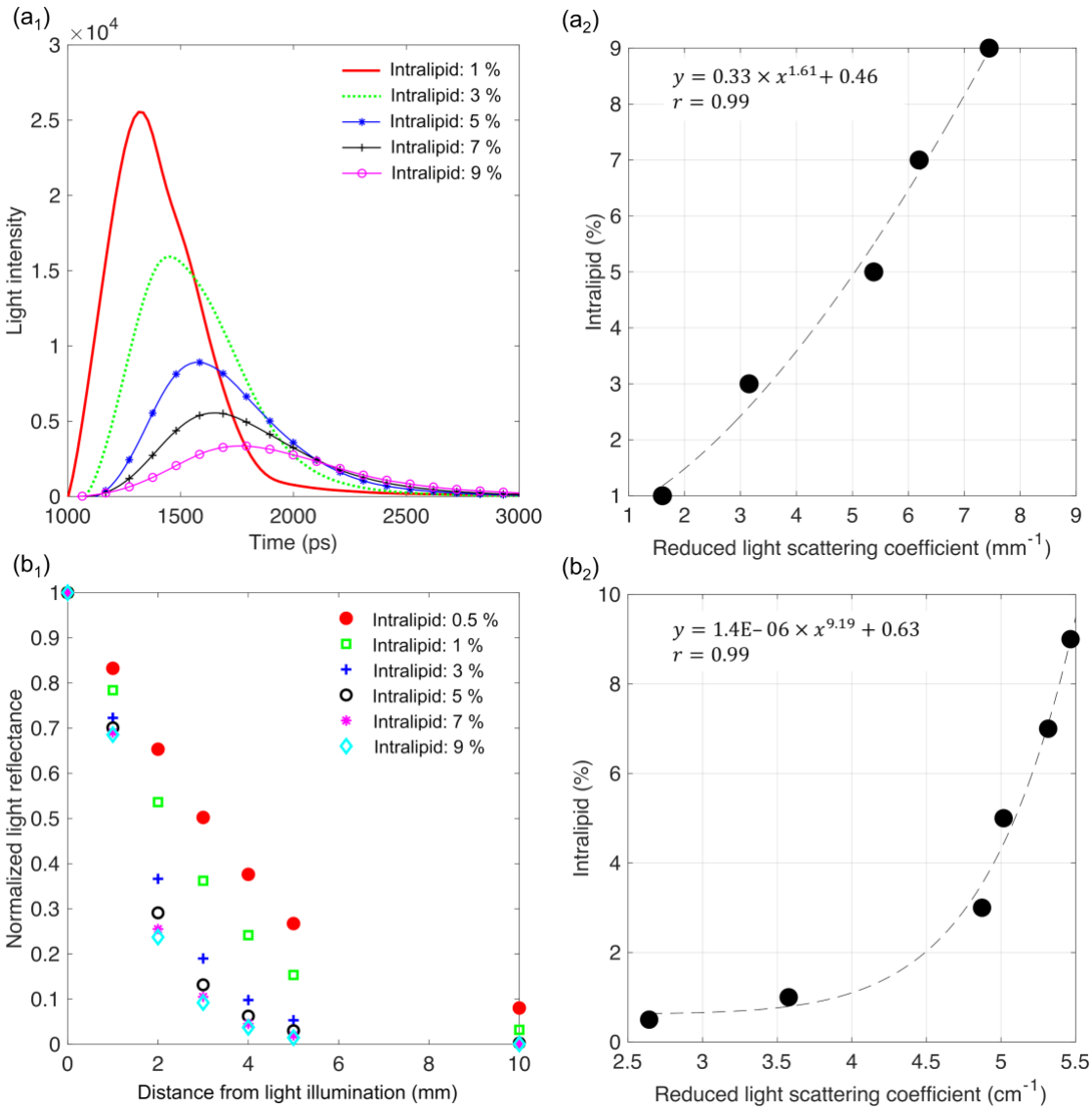

Figure 2. Time- (a_1) and spatially (b_1) resolved profiles at wavelength 846 nm collected from the intralipid scatters. The estimated μ_s' values by the time- (a_2) and spatially (b_2) resolved spectroscopy.

Figure 3 (a-c) show the correlation between the estimated coefficients based on exponential decay and the intralipid contents. A positive correlation was found between coefficient b and the intralipid contents. Additionally, regression analysis could improve the correlation between predicted intralipid contents and their reference values (Figure 3 (d)). It suggests that such a direct data analysis approach can be used to investigate the light scattering characteristics acquired by the designed SRS system.

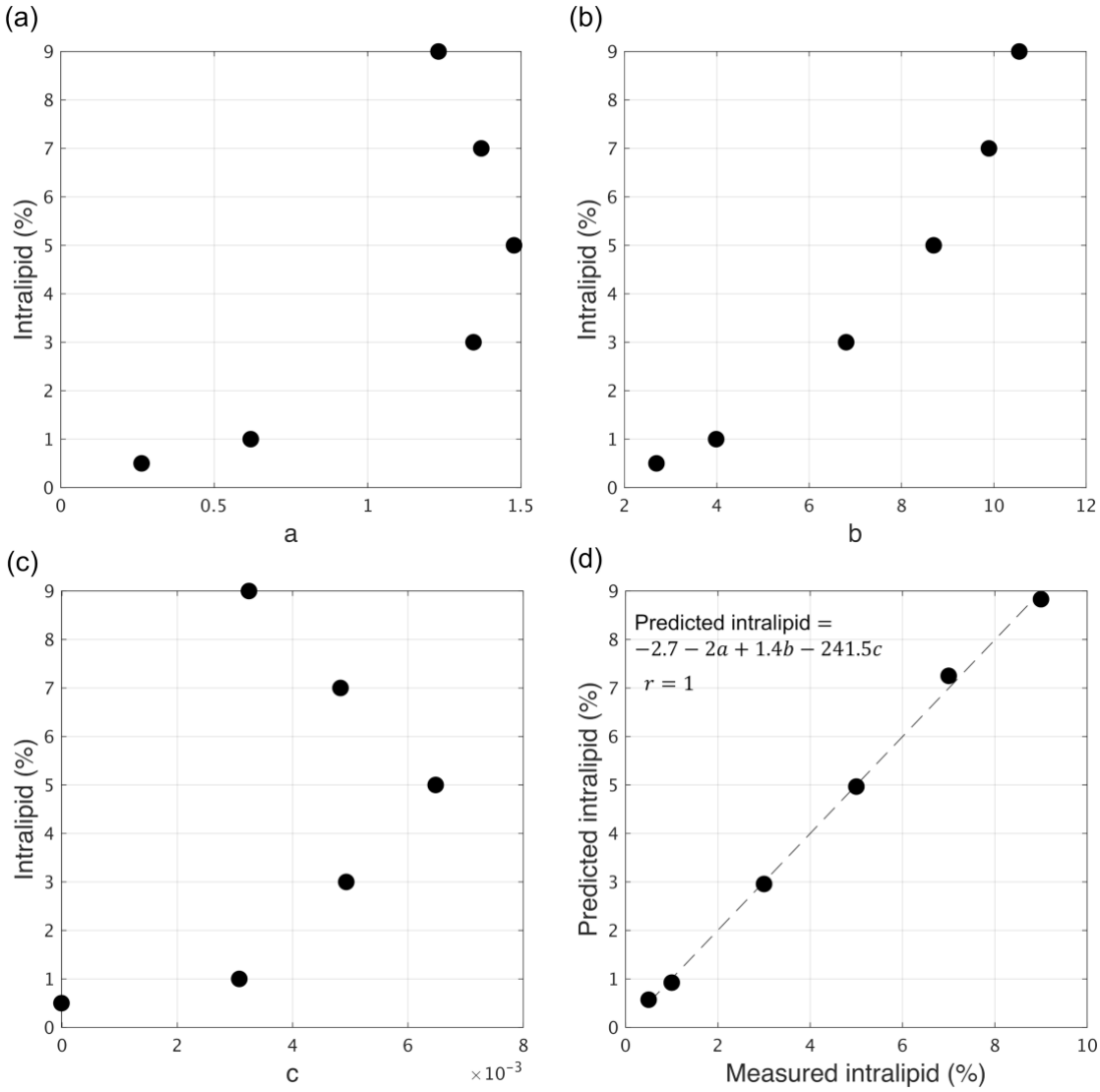

Figure 3. (a-c) The correlation between the estimated coefficients and the intralipid contents. (d) The scatter plot between the predicted and measured intralipid contents.

Table 2 summarizes the firmness, SSC, and pH reference values of all 120 included kiwifruits. The correlation coefficient between the firmness and pH was –0.46 (see supplementary information), suggesting the possibility of creating dependent prediction models for firmness and pH. Conversely, the correlations between firmness and SSC, between pH and SSC were extremely low, suggesting the necessity for constructing independent prediction models for SSC.

Table 2. Summary of the firmness, SSC, pH, and equatorial diameter reference values.

	Min	**Max**	**Mean**	**SD**
Firmness (N/cm^2)	29.96	55.60	41.94	6.05
SSC (%)	14.30	21.30	17.18	1.53
pH (%)	3.35	4.70	3.93	0.26
Equatorial diameter (mm)	52	63	56	2

SSC: soluble solids content; Min: minimum measured value; Max: maximum measured value; SD: standard deviation

Figure 4 shows the compression test simulation results at 0, 1, 2, and 3 s, stress was selected as the display option. The stress of kiwifruit increased significantly when the elastic modulus of the sarcocarp expanded. This reflects that the firmness of kiwifruit had been significantly increased. Thus, measuring the kiwifruit with the pericarp was considered an acceptable method in this study.

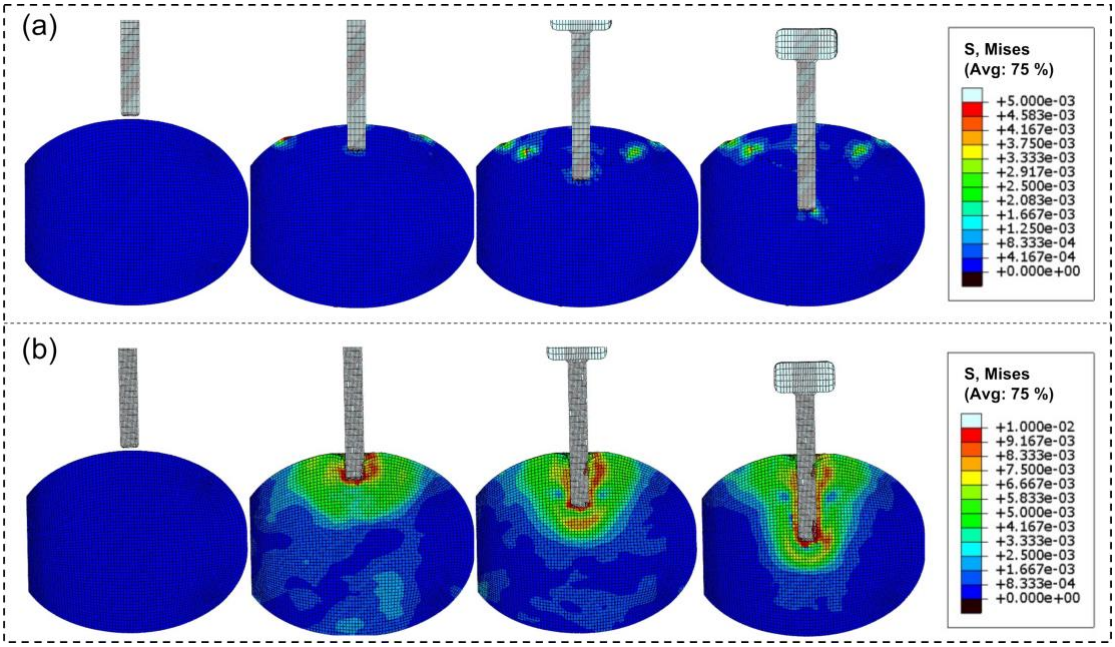

Figure 4. Compression simulation results at 0, 1, 2, and 3 s for (a) soft and (b) firm samples.

Figure 5 shows the mean spectra plotted with one standard error bar collected from kiwifruits with different firmness levels at the same light wavelength of 846 nm (a: TRP; b: SRP). Firmer samples tended to reflect a lower transmitted light intensity. Berardinelli et al. (2019) indicated the same phenomenon that more light passes through the softer kiwifruit. Additionally, by checking the light reflectance values earned by the SRS method, it was found that more light was lost in the firmer samples from the light illumination spot. Both methods could support the same view, i.e., firmer kiwifruit samples tended to have higher light scattering inside.

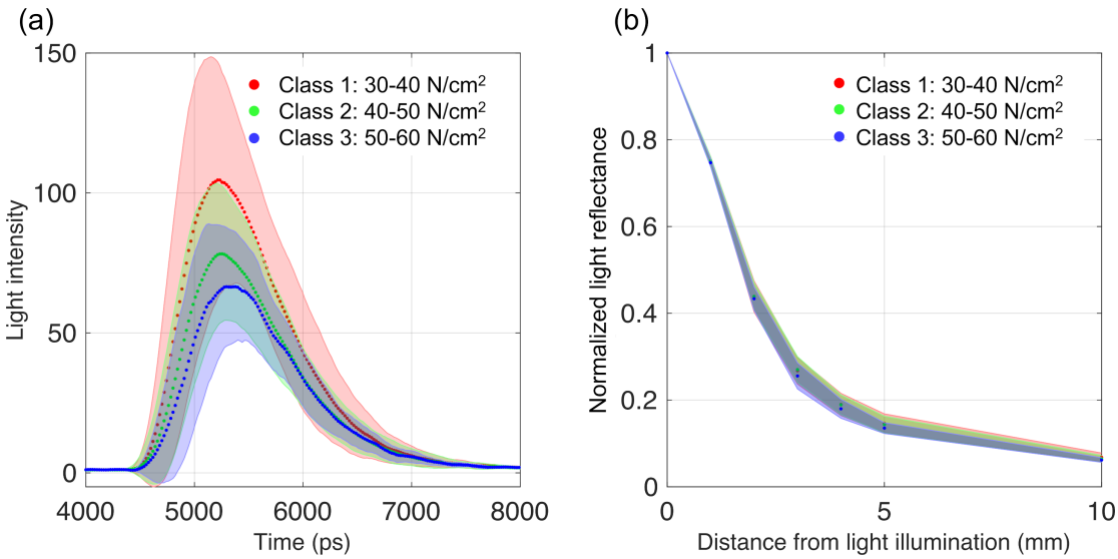

Figure 5. Mean spectra were plotted with one standard error bar collected from all 120 kiwifruit samples and sorted into three classes by firmness reference values (time- (a) and spatially (b) resolved profiles).

Figure 6 shows the correlation between kiwifruit properties and the optical properties at a single wavelength of 846 nm derived using the TRS method. The observations were as follows: (1) Expectedly, the FWHM value positively correlated with the sample firmness, whereas the transmitted light intensity (i.e., the peak area) was negatively correlated with the same firmness reference values. This suggests that the light scattering in firmer samples was larger than in softer ones. The reduced scattering coefficients fitted by the inverse algorithm could represent the characteristics of the raw data. (2) There was an extremely low correlation between the optical properties and the SSC reference values, suggesting the difficulty of using light scattering properties at 846 nm to predict the SSC values. (3) The FWHM value and light intensity showed a good correlation with the pH reference values. The negative correlation between the fruit firmness and pH values may have contributed to this result.

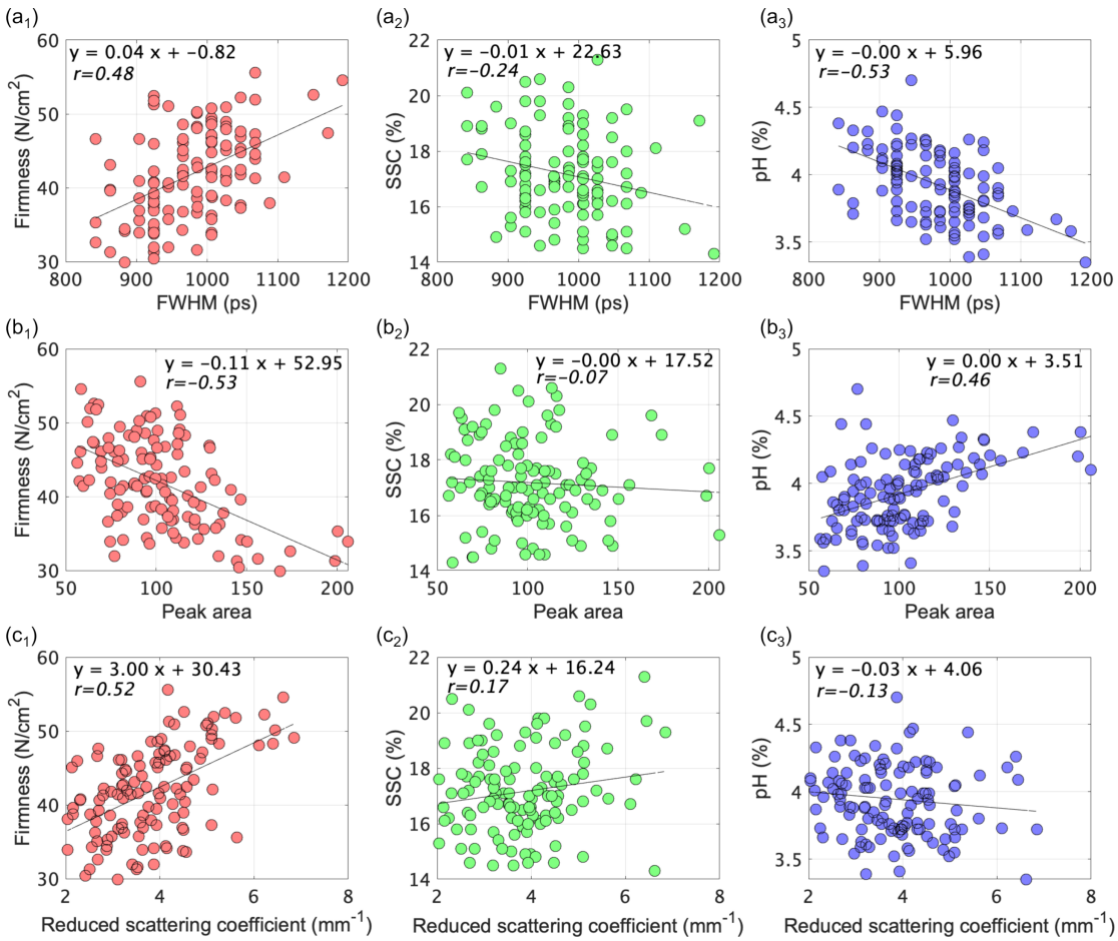

Figure 6. Correlation between kiwifruit properties and the optical properties derived using the time-resolved spectroscopy.

Figure 7 (a) shows the correlation between kiwifruit properties and the optical properties at the same wavelength of 846 nm derived using the SRS method. The estimated μ_s'(SRS) were positively correlated with sample firmness, suggesting the SRS approach could be an alternative to estimate light scattering characteristics in kiwifruit. The estimated μ_s'(SRS) of the kiwifruits were lower than 2 % intralipid, whereas the μ_s'(TRS) values were much higher than this value. This could partly be explained by the transmission-type TRS may have evaluated the optical preparties in the sample with skin more robustly than reflectance-type SRS. Another possible reason is that the TRS measured the middle part of kiwifruit (i.e., including the placenta and seed chamber) simultaneously. In contrast, the SRS method only measured the sub-surface parts. Fang et al. (2016) showed significant differences among the

μ_s' of the different parts of kiwifruit. Figure 7 (b) shows the correlation between kiwifruit properties and their predicted results using the estimated coefficients. The correlation coefficients for the firmness, SSC, and pH were 0.56, 0.33, and 0.56, respectively, higher than that using the μ_s'(SRS).

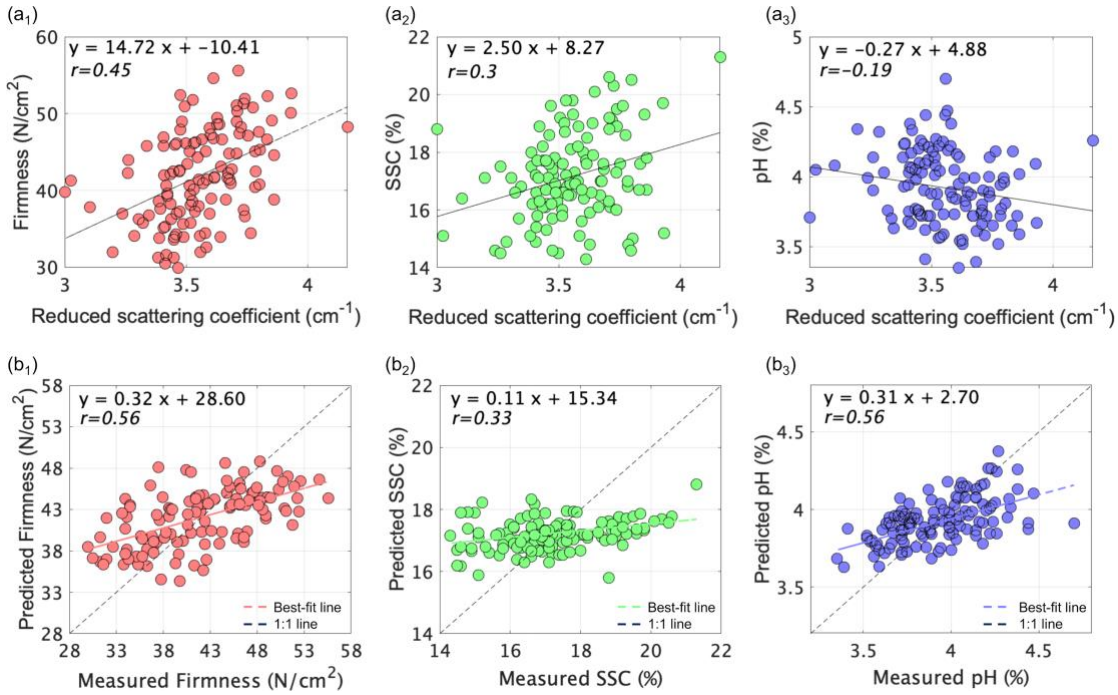

Figure 7. (a) Correlation between kiwifruit properties and the μ_s' derived using the spatially resolved spectroscopy. (b) Scatter plot between the measured kiwifruit properties and their predicted values using the direct data analysis approach.

Since simultaneous multiwavelength measurements were made by the designed Vis–NIR SRS system, multivariate regression analysis was further tested for the quality evaluation of kiwifruit. Figure 8 (a_1) shows the mean curve-fitted parameters a, b, and c with their one standard error bar collected from the calibration set of samples. The dark circles plotted on each mean spectrum indicated CARS-selected wavelengths. Figure 8 (a_2) shows the PLS regression coefficients. The light scattering information with less absorption effects (in the 850-900 nm region) and water absorption (in the 900-1000 nm region) were mainly selected for firmness prediction. Figure 8 (a_3) shows a scatter plot of firmness reference values and their predicted values by PLS regression analysis, which were highly correlated with R_{cal}^2 and

$RMSE_{cal}$ was 0.71 and 3.24 N/cm^2 under five-fold cross-validation for the calibration set. For the validation set, R^2_{val} and $RMSE_{val}$ was 0.64 and 3.63 N/cm^2, respectively. Although it was difficult to make a direct comparison with previous studies, based on the variety of sample preparations and data analysis methods that were applied, the overall prediction statistics for firmness in this study were comparable with that in the research that used the reflectance-type TRS method, in which the classification accuracy for the firmness of kiwifruits (divided into three groups) was 75 % (Valero et al., 2004). The SSC calibration model had a good prediction accuracy; the R^2_{cal} and $RMSE_{cal}$ of the calibration set were 0.7 and 0.8 %, respectively. And the R^2_{val} and $RMSE_{val}$ of the validation set were 0.67 and 0.95 % (Figure 8 ($b_{1\text{-}3}$)). However, the SSC prediction results were inferior to those noted in existing NIR spectroscopy studies (McGlone et al., 2002; McGlone and Kawano, 1998; Moghimi et al., 2010; Slaughter and Crisosto, 1998). The predicted results of pH (Figure 8 ($c_{1\text{-}3}$)) showed calibration accuracy with an R^2_{cal} of 0.59 ($RMSE_{cal}$ = 0.17 %) under the same five-fold cross-validation as for the calibration set; contrastingly, the R^2_{val} decreased sharply to 0.38. Nevertheless, the $RMSE_{val}$ (0.19 %) was close to the value of the $RMSE_{cal}$, suggesting the possibility of using the SRS system to estimate pH values. However, more work is required to prove this.

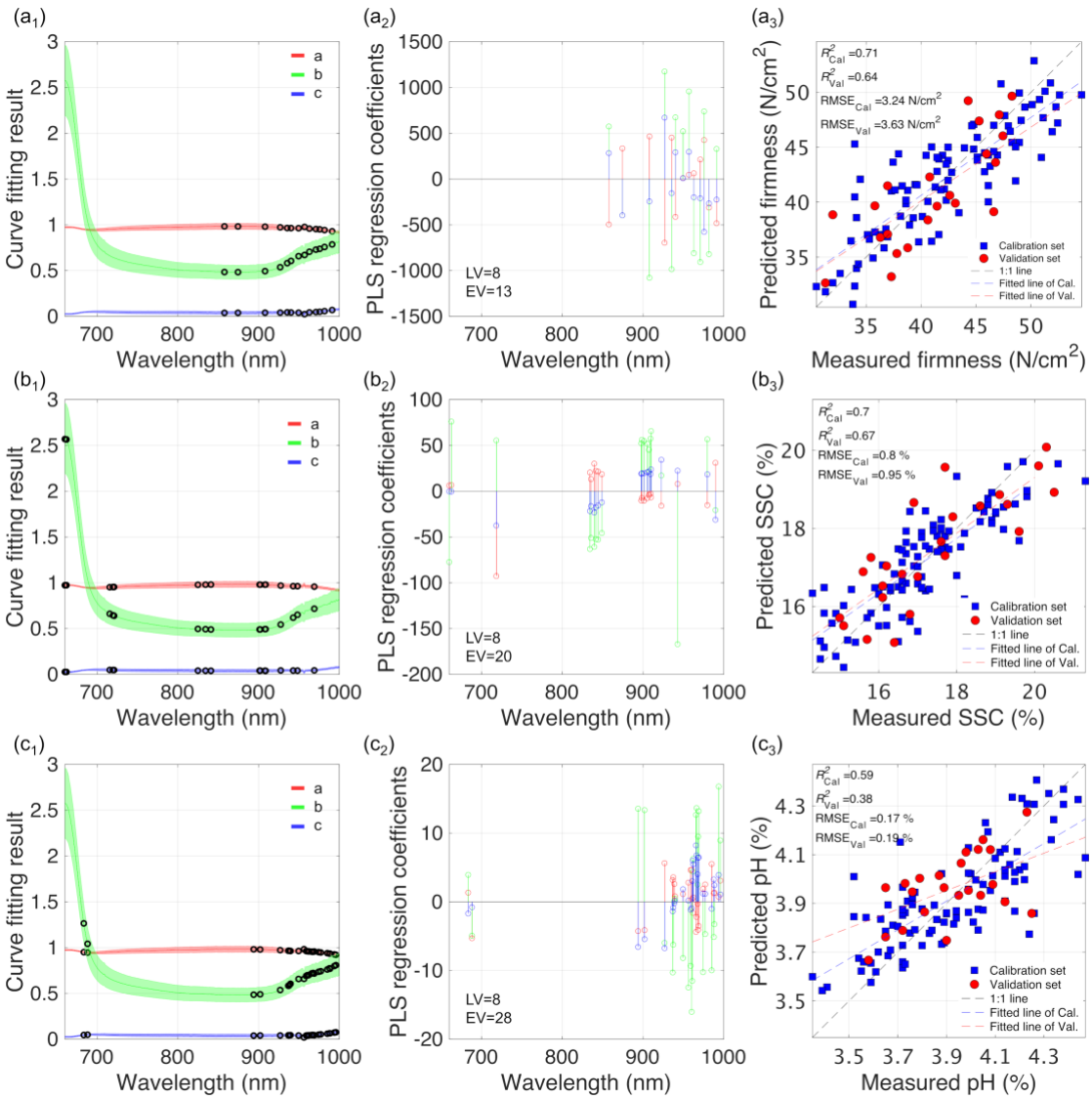

Figure 8. Calibration results of kiwifruit (a) firmness, (b) soluble solids content, and (c) pH using the designed hyperspectral imaging-based spatially resolved system coupled with partial least squares regression analysis.

The presented calibration results were also benchmarked against the standard diffuse reflectance spectroscopy results of one fiber-group position of the same SRS system to quantify the added value of using the SRS approach. Figure 9 ($a_{1\text{-}3}$) shows the raw NIR spectra with one standard error bar collected by the 1-mm, 2-mm, and 3-mm FG, respectively. No spectral pretreatments were used to retain the light scattering effects. The dark circles plotted on each mean spectrum indicate the wavelengths selected using CARS. Figures 9 ($b_{1\text{-}3}$) and ($c_{1\text{-}3}$) show the PLS regression coefficients and the calibration results, respectively. Table

1 summarizes the predicted results of firmness by other FGs. The most robust calibration model was constructed by the 1-mm FG when using 31 wavelengths, and the lowest RMSE for five-fold cross-validation was achieved when the LV = 7. The firmness prediction accuracy was R^2_{cal} = 0.37 and $RMSE_{cal}$ = 4.75 N/cm^2. The R^2_{val} and $RMSE_{val}$ were 0.38 and 4.76 N/cm^2, respectively. Overall, it was evident that the SRS approach achieved higher accuracies for kiwifruit firmness prediction than the standard diffuse reflectance spectroscopy when using the same measuring system.

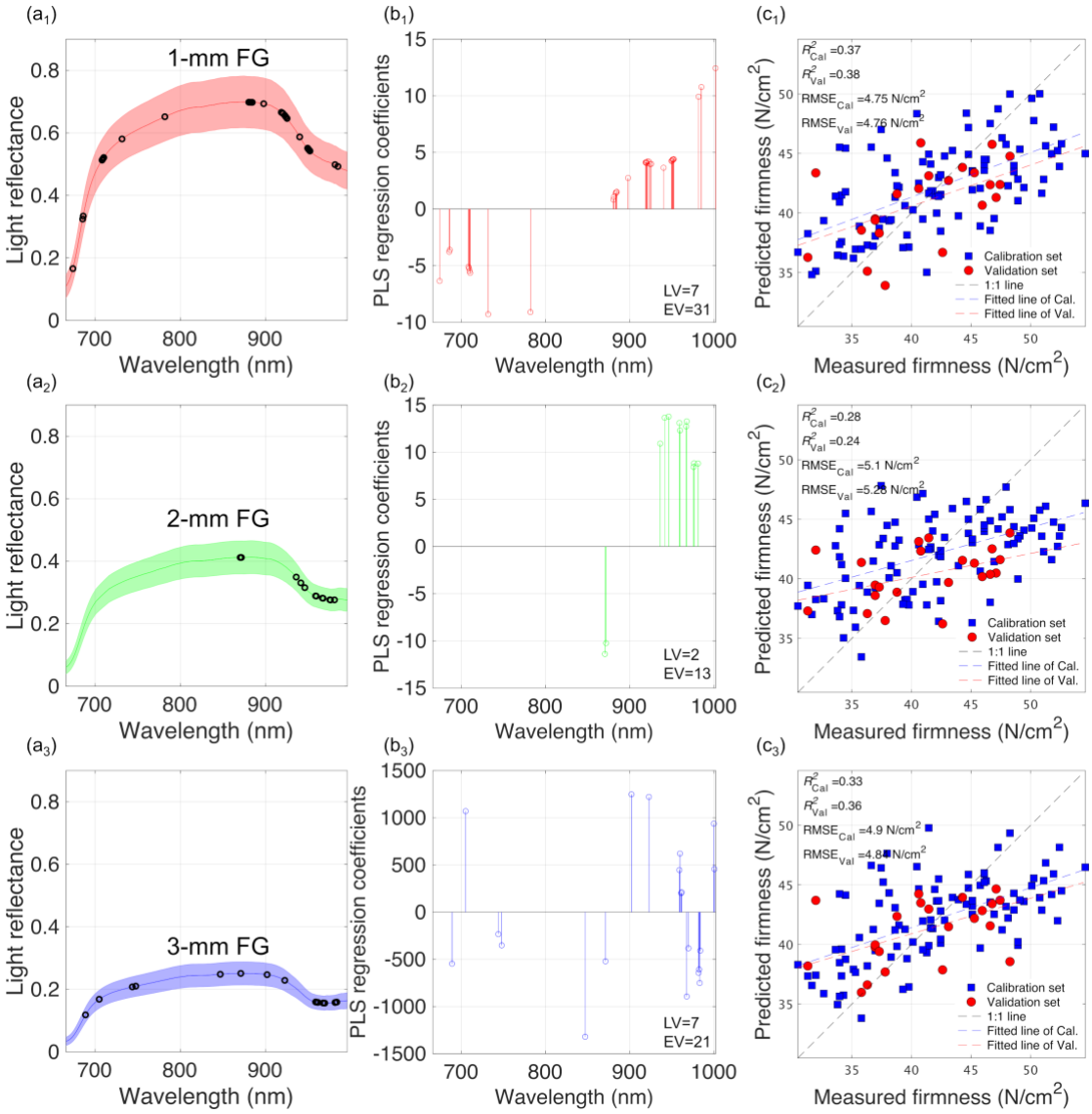

Figure 9: (a) Near-infrared spectra of kiwifruit at various firmness. (b) Partial least squares regression coefficients. (c) Scatter plots of the measured and predicted firmness.

Figure 10 ($a_{1\text{-}3}$) shows the NIR spectra with one standard error bar collected by the 1-mm, 2-mm, and 3-mm FG, respectively. Except for the same spectral pretreatments as the SRS data analysis, the SNV was used to reduce the light scattering effects (Kobori et al., 2013). Figure 10 ($b_{1\text{-}3}$) shows the PLS regression coefficients. Since the kiwifruit samples were purchased at the same commercial maturity stage, the information of chlorophyll content (in the 660-700 nm region) was likely less useful compared to water content for the construction of the SSC calibration model. Figure 10 ($c_{1\text{-}3}$) shows the scatter plot of the measured SSC and their predicted values using PLS regression analysis. Table 1 summarizes the calibration results of SSC by other FGs. The best performing PLS calibration model could achieve R^2_{cal} = 0.81 and $RMSE_{cal}$ = 0.65 % when using the spectra collected by the 1-mm FG. R^2_{val} and $RMSE_{val}$ were 0.69 and 0.93 % for the validation set, respectively. The 2-mm FG could also achieve comparable prediction accuracies to that of the 1-mm FG. The performance for predicting SSC by the standard diffuse reflectance spectroscopy was confirmed to be better than that of the direct SRS data analysis. This suggests that light scattering information was less useful for the SSC prediction.

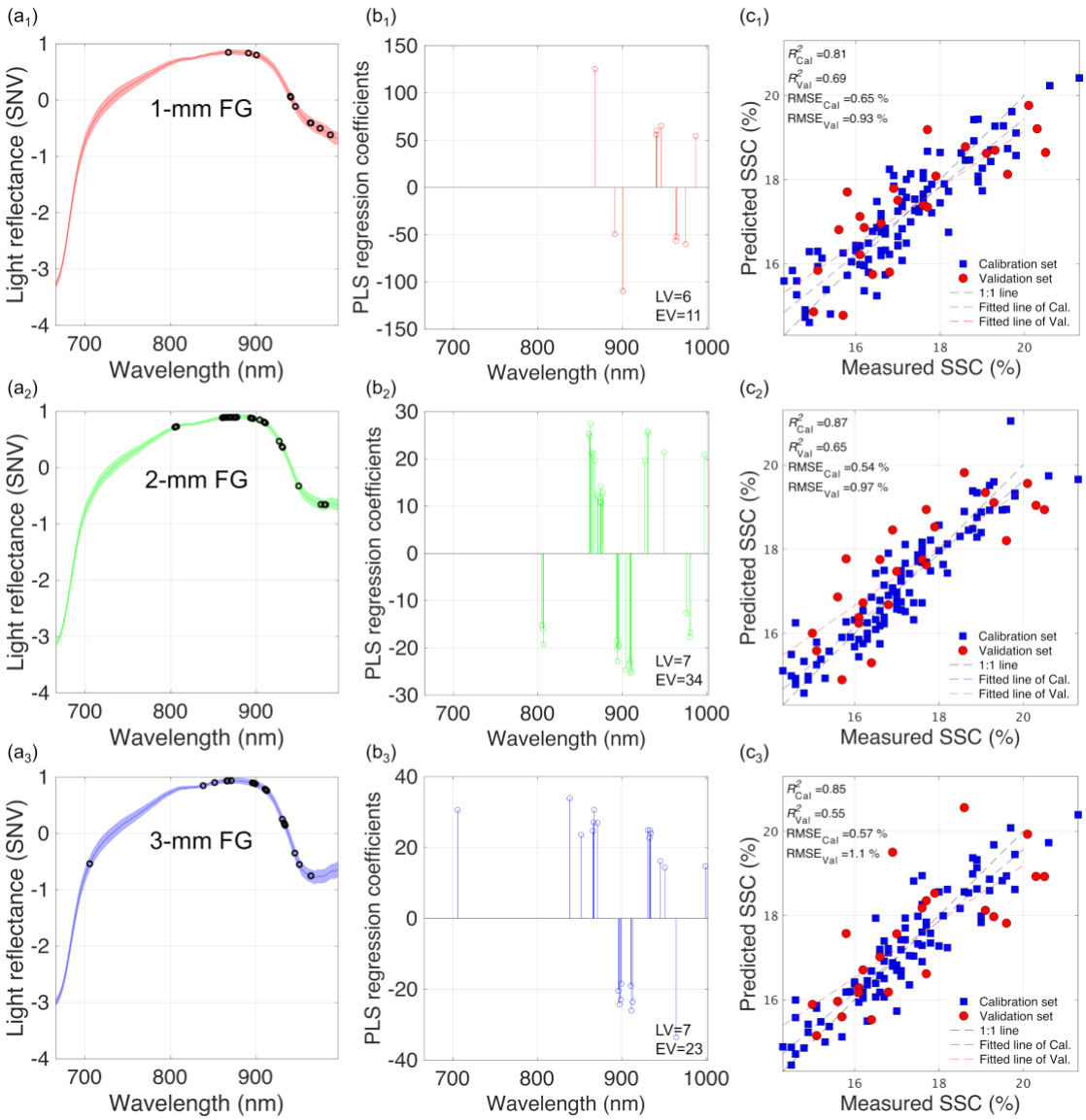

Figure 10: (a) Pretreated near-infrared spectra of kiwifruit. (b) Partial least squares regression coefficients. (c) Scatter plots of the measured and predicted soluble solids content.

Table 1. Firmness (N/cm^2) and SSC (%) prediction results of calibration and validation sets using the 4-mm, 5-mm, and 10-mm fiber group, respectively.

	Reference fiber group: 4-mm				Reference fiber group: 5-mm				Reference fiber group: 10-mm			
	R^2_{cal}	$RMSE_{cal}$	R^2_{val}	$RMSE_{val}$	R^2_{cal}	$RMSE_{cal}$	R^2_{val}	$RMSE_{val}$	R^2_{cal}	$RMSE_{cal}$	R^2_{val}	$RMSE_{val}$
Firmness (N/cm^2)	0.37	4.77	0.25	5.24	0.33	4.91	0.3	5.07	0.17	5.47	0.08	5.8
SSC (%)	0.88	0.52	0.59	1.06	0.87	0.53	0.56	1.1	0.84	0.59	0.58	1.07

Note: R^2 is the coefficient of determination. RMSE is the root mean square error. SSC is the soluble solids content.

4. Conclusion

This study aimed to demonstrate a nondestructive and rapid SRS method for predicting the firmness, SSC, and pH in kiwifruit. TRS was used to validate light scattering characteristics at a single wavelength of 846 nm inside samples using transmission measurements; the results showed that firmer kiwifruits had higher light scattering inside. The SRS method confirmed the light scattering characteristics and was subsequently used to test the prediction of sample properties. The PLS calibration results were benchmarked against standard diffuse reflectance spectroscopy results from one fiber group position of the same SRS system. Compared with conventional NIR studies, the multifiber-based Vis-NIR SRS measurement system offered observable advantages for predicting the firmness of kiwifruit. Further research should focus on extending the applicability of the SRS approach to a broader database of kiwifruit types. Moreover, more effective designs of the SRS system and either direct or indirect data analysis methods must be continuously developed.

5. Acknowledgment

The authors gratefully thank the financial support provided by JSPS (KAKENHI, No. 19H03015 and No.19K15886) and China Scholarship Council (CSC, No. 202006300096).

6. Reference

Adebayo, S.E., Hashim, N., Hass, R., Reich, O., Regen, C., Münzberg, M., Abdan, K., Hanafi, M., Zude-Sasse, M., 2017. Using absorption and reduced scattering coefficients for non-destructive analyses of fruit flesh firmness and soluble solids content in pear (Pyrus communis 'Conference')—An update when using diffusion theory. Postharvest Biol. Technol. 130, 56–63. https://doi.org/10.1016/j.postharvbio.2017.04.004

Aernouts, B., Zamora-Rojas, E., Van Beers, R., Watté, R., Wang, L., Tsuta, M., Lammertyn, J., Saeys, W., 2013. Supercontinuum laser based optical characterization of Intralipid® phantoms in the 500-2250 nm range. Opt. Express 21, 32450. https://doi.org/10.1364/oe.21.032450

Antunes, M.D.C., Pateraki, I., Kanellis, A.K., Sfakiotakis, E.M., 2000. Differential effects of low-temperature inhibition on the propylene induced autocatalysis of ethylene production, respiration and ripening of "Hayward" kiwifruit. J. Hortic. Sci. Biotechnol. 75, 575–580. https://doi.org/10.1080/14620316.2000.11511288

Asiche, W.O., Mitalo, O.W., Kasahara, Y., Tosa, Y., Mworia, E.G., Ushijima, K., Nakano, R., Kubo, Y., 2017. Effect of storage temperature on fruit ripening in three kiwifruit cultivars. Hortic. J. 86, 403–410. https://doi.org/10.2503/hortj.OKD-028

Ban, M., Inagaki, T., Ma, T., Tsuchikawa, S., 2018. Effect of cellular structure on the optical properties of wood. J. Near Infrared Spectrosc. 26, 53–60.

https://doi.org/10.1177/0967033518757233
Baranyai, L., Zude, M., 2009. Analysis of laser light propagation in kiwifruit using backscattering imaging and Monte Carlo simulation. Comput. Electron. Agric. 69, 33–39. https://doi.org/10.1016/j.compag.2009.06.011
Berardinelli, A., Benelli, A., Tartagni, M., Ragni, L., 2019. Kiwifruit flesh firmness determination by a NIR sensitive device and image multivariate data analyses. Sensors Actuators, A Phys. 296, 265–271. https://doi.org/10.1016/j.sna.2019.07.027
Brummell, D.A., Harpster, M.H., 2001. Cell wall metabolism in fruit softening and quality and its manipulation in transgenic plants, in: Plant Cell Walls. Springer, pp. 311–340.
Cen, H., Lu, R., 2010. Optimization of the hyperspectral imaging-based spatially-resolved system for measuring the optical properties of biological materials. Opt. Express 18, 17412. https://doi.org/10.1364/oe.18.017412
Cen, H., Lu, R., Mendoza, F.A., Ariana, D.P., 2012. Assessing Multiple Quality Attributes of Peaches Using Optical Absorption and Scattering Properties. Trans. ASABE 55, 647–657. https://doi.org/10.13031/2013.41366
Chapman, G.W., Horvat, R.J., 1990. Changes in Nonvolatile Acids, Sugars, Pectin, and Sugar Composition of Pectin during Peach (Cv. Monroe) Maturation. J. Agric. Food Chem. 38, 383–387. https://doi.org/10.1021/jf00092a008
Ciccoritti, R., Paliotta, M., Amoriello, T., Carbone, K., 2019. FT-NIR spectroscopy and multivariate classification strategies for the postharvest quality of green-fleshed kiwifruit varieties. Sci. Hortic. (Amsterdam). 257. https://doi.org/10.1016/j.scienta.2019.108622
De Belie, N., Tu, K., Jancsók, P., De Baerdemaeker, J., 1999. Preliminary study on the influence of turgor pressure on body reflectance of red laser light as a ripeness indicator for apples. Postharvest Biol. Technol. 16, 279–284. https://doi.org/10.1016/S0925-5214(99)00025-3
Fang, Z. huan, Fu, X. ping, He, X. ming, 2016. Investigation of absorption and scattering characteristics of kiwifruit tissue using a single integrating sphere system. J. Zhejiang Univ. Sci. B 17, 484–492. https://doi.org/10.1631/jzus.B1500086
Farrell, T.J., Patterson, M.S., Brain, W., 1992. A diffusion theory model of spatially resolved, steady-state diffuse reflectance for the noninvasive determination of tissue optical properties in vivo. Medphys 19, 879–888. https://doi.org/10.1118/1.596777
Fu, X., Ying, Y., Lu, H., Xu, H., Yu, H., 2007. FT-NIR diffuse reflectance spectroscopy for kiwifruit firmness detection. Sens. Instrum. Food Qual. Saf. 1, 29–35. https://doi.org/10.1007/s11694-007-9004-2
Giovanelli, G., Sinelli, N., Beghi, R., Guidetti, R., Casiraghi, E., 2014. NIR spectroscopy for the optimization of postharvest apple management. Postharvest Biol. Technol. 87, 13–20. https://doi.org/10.1016/j.postharvbio.2013.07.041
Goldberg, T., Agra, H., Ben-Arie, R., 2019. Non-destructive measurement of fruit firmness to predict the shelf-life of 'Hayward' kiwifruit. Sci. Hortic. (Amsterdam). 244, 339–342. https://doi.org/10.1016/j.scienta.2018.09.057
Guo, W., Zhao, F., Dong, J., 2016. Nondestructive Measurement of Soluble Solids Content of Kiwifruits Using Near-Infrared Hyperspectral Imaging. Food Anal. Methods 9, 38–47. https://doi.org/10.1007/s12161-015-0165-z
Hielscher, A.H., Jacques, S.L., Wang, L., Tittel, F.K., 1995. The influence of boundary conditions on the accuracy of diffusion theory in time-resolved reflectance spectroscopy of biological tissues. Phys. Med. Biol. 40, 1957–1975. https://doi.org/10.1088/0031-9155/40/11/013
Hjalmarsson, P., Thennadil, S.N., 2007. Spatially resolved in vivo measurement system for estimating the optical properties of tissue in the wavelength range 1000-1700 nm, in: Proc. SPIE 6628, Diagnostic Optical Spectroscopy in Biomedicine IV, 662805. https://doi.org/10.1117/12.728183
Huang, H., Liu, L., Ngadi, M.O., 2014. Recent developments in hyperspectral imaging for assessment of food quality and safety. Sensors (Switzerland) 14, 7248–7276. https://doi.org/10.3390/s140407248

Huang, Y., Lu, R., Chen, K., 2017. Development of a multichannel hyperspectral imaging probe for property and quality assessment of horticultural products. Postharvest Biol. Technol. 133, 88–97. https://doi.org/10.1016/j.postharvbio.2017.07.009

Huang, Y., Lu, R., Hu, D., Chen, K., 2018. Quality assessment of tomato fruit by optical absorption and scattering properties. Postharvest Biol. Technol. 143, 78–85. https://doi.org/10.1016/j.postharvbio.2018.04.016

Kobori, H., Gorretta, N., Rabatel, G., Bellon-Maurel, V., Chaix, G., Roger, J.M., Tsuchikawa, S., 2013. Applicability of Vis-NIR hyperspectral imaging for monitoring wood moisture content (MC). Holzforschung 67, 307–314. https://doi.org/10.1515/hf-2012-0054

Konagaya, K., Inagaki, T., Kitamura, R., Tsuchikawa, S., 2016. Optical properties of drying wood studied by time-resolved near-infrared spectroscopy. Opt. Express 24, 9561. https://doi.org/10.1364/OE.24.009561

Li, H., Liang, Y., Xu, Q., Cao, D., 2009. Key wavelengths screening using competitive adaptive reweighted sampling method for multivariate calibration. Anal. Chim. Acta 648, 77–84. https://doi.org/10.1016/j.aca.2009.06.046

Li, M., Verboven, P., Buchsbaum, A., Cantre, D., Nicolaï, B., Heyes, J., Mowat, A., East, A., 2015. Characterising kiwifruit (Actinidia sp.) near skin cellular structures using optical coherence tomography. Postharvest Biol. Technol. 110, 247–256. https://doi.org/10.1016/j.postharvbio.2015.08.021

Lu, R., Van Beers, R., Saeys, W., Li, C., Cen, H., 2020. Measurement of optical properties of fruits and vegetables: A review. Postharvest Biol. Technol. 159, 111003. https://doi.org/10.1016/j.postharvbio.2019.111003

Ma, T., Li, X., Inagaki, T., Yang, H., Tsuchikawa, S., 2018a. Noncontact evaluation of soluble solids content in apples by near-infrared hyperspectral imaging. J. Food Eng. 224, 53–61. https://doi.org/10.1016/j.jfoodeng.2017.12.028

Ma, T., Schajer, G., Inagaki, T., Pirouz, Z., Tsuchikawa, S., 2018b. Optical characteristics of Douglas fir at various densities, grain directions and thicknesses investigated by near-infrared spatially resolved spectroscopy (NIR-SRS). Holzforschung 1–8. https://doi.org/10.1515/hf-2017-0213

Ma, T., Xia, Y., Inagaki, T., Tsuchikawa, S., 2021. Rapid and nondestructive evaluation of soluble solids content (SSC) and firmness in apple using Vis–NIR spatially resolved spectroscopy. Postharvest Biol. Technol. 173. https://doi.org/10.1016/j.postharvbio.2020.111417

Magwaza, L.S., Opara, U.L., 2015. Analytical methods for determination of sugars and sweetness of horticultural products-A review. Sci. Hortic. (Amsterdam). 184, 179–192. https://doi.org/10.1016/j.scienta.2015.01.001

Martelli, F., Contini, D., Taddeucci, A., Zaccanti, G., 1997. Photon migration through a turbid slab described by a model based on diffusion approximation II Comparison with Monte Carlo results. Appl. Opt. 36, 4600. https://doi.org/10.1364/ao.36.004600

Martelli, F., Del Bianco, S., Ismaelli, A., 2009. Light propagation through biological tissue and other diffusive media: theory, solutions, and software. Society of Photo-Optical Instrumentation Engineers.

Martens, H., Tormod, N., 1992. Multivariate calibration. John Wiley & Sons.

McGlone, V.A., Abe, H., Kawano, S., 1997. Kiwifruit firmness by near infrared light scattering. J. Near Infrared Spectrosc. 5, 83–89. https://doi.org/10.1255/jnirs.102

McGlone, V.A., Clark, C.J., Jordan, R.B., 2007. Comparing density and VNIR methods for predicting quality parameters of yellow-fleshed kiwifruit (Actinidia chinensis). Postharvest Biol. Technol. 46, 1–9. https://doi.org/10.1016/j.postharvbio.2007.04.003

McGlone, V.A., Jordan, R.B., Seelye, R., Martinsen, P.J., 2002. Comparing density and NIR methods for measurement of Kiwifruit dry matter and soluble solids content. Postharvest Biol. Technol. 26, 191–198. https://doi.org/10.1016/S0925-5214(02)00014-5

McGlone, V.A., Kawano, S., 1998. Firmness, dry-matter and soluble-solids assessment of postharvest kiwifruit by NIR spectroscopy. Postharvest Biol. Technol. 13, 131–141. https://doi.org/10.1016/S0925-5214(98)00007-6

Michels, R., Foschum, F., Kienle, A., 2008. Optical properties of fat emulsions. Opt. Express

16, 5907. https://doi.org/10.1364/oe.16.005907
Moghimi, A., Aghkhani, M.H., Sazgarnia, A., Sarmad, M., 2010. Vis/NIR spectroscopy and chemometrics for the prediction of soluble solids content and acidity (pH) of kiwifruit. Biosyst. Eng. 106, 295–302. https://doi.org/10.1016/j.biosystemseng.2010.04.002
Moughan, P.J., Rutherfurd, S.M., Balan, P., 2013. Chapter Nine - Kiwifruit, Mucins, and the Gut Barrier, in: Boland, M., Moughan, P.J. (Eds.), Nutritional Benefits of Kiwifruit, Advances in Food and Nutrition Research. Academic Press, pp. 169–185. https://doi.org/https://doi.org/10.1016/B978-0-12-394294-4.00009-2
Nicolaï, B.M., Beullens, K., Bobelyn, E., Peirs, A., Saeys, W., Theron, K.I., Lammertyn, J., 2007. Nondestructive measurement of fruit and vegetable quality by means of NIR spectroscopy: A review. Postharvest Biol. Technol. 46, 99–118. https://doi.org/10.1016/j.postharvbio.2007.06.024
Peng, Y., Lu, R., 2008. Analysis of spatially resolved hyperspectral scattering images for assessing apple fruit firmness and soluble solids content. Postharvest Biol. Technol. 48, 52–62. https://doi.org/10.1016/j.postharvbio.2007.09.019
Peng, Y., Lu, R., 2005. Modeling multispectral scattering profiles for prediction of apple fruit firmness. Trans. Am. Soc. Agric. Eng. 48, 235–242. https://doi.org/10.13031/2013.17923
Qin, J., Lu, R., 2008. Measurement of the optical properties of fruits and vegetables using spatially resolved hyperspectral diffuse reflectance imaging technique. Postharvest Biol. Technol. 49, 355–365. https://doi.org/10.1016/j.postharvbio.2008.03.010
Qin, J., Lu, R., Peng, Y., 2009. Prediction of apple internal quality using spectral absorption and scattering properties. Trans. ASABE 52, 486–499. https://doi.org/10.13031/2013.26807
Rizzolo, A., Vanoli, M., Bianchi, G., Zanella, A., Grassi, M., Torricelli, A., Spinelli, L., 2014. Relationship between texture sensory profiles and optical properties measured by time-resolved reflectance spectroscopy during post-storage shelf life of “Braeburn” apples. J. Hortic. Res. 22, 113–121. https://doi.org/10.2478/johr-2014-0014
Rogel-Castillo, C., Boulton, R., Opastpongkarn, A., Huang, G., Mitchell, A.E., 2016. Use of Near-Infrared Spectroscopy and Chemometrics for the Nondestructive Identification of Concealed Damage in Raw Almonds (Prunus dulcis). J. Agric. Food Chem. 64, 5958–5962. https://doi.org/10.1021/acs.jafc.6b01828
Romano, G., Nagle, M., Argyropoulos, D., Müller, J., 2011. Laser light backscattering to monitor moisture content, soluble solid content and hardness of apple tissue during drying. J. Food Eng. 104, 657–662. https://doi.org/10.1016/j.jfoodeng.2011.01.026
Santagapita, P.R., Tylewicz, U., Panarese, V., Rocculi, P., Dalla Rosa, M., 2016. Non-destructive assessment of kiwifruit physico-chemical parameters to optimise the osmotic dehydration process: A study on FT-NIR spectroscopy. Biosyst. Eng. 142, 101–109. https://doi.org/10.1016/j.biosystemseng.2015.12.011
Shmulevich, I., Galili, N., Howarth, M.S., 2003. Nondestructive dynamic testing of apples for firmness evaluation. Postharvest Biol. Technol. 29, 287–299. https://doi.org/10.1016/S0925-5214(03)00039-5
Slaughter, D.C., Crisosto, C.H., 1998. Nondestructive internal quality assessment of kiwifruit using near-infrared spectroscopy. Semin. Food Anal. 3, 131–140.
Sun, C., Aernouts, B., Saeys, W., 2021. Bridging the gap between measurement-based and simulation-based metamodels for deriving bulk optical properties from spatially-resolved reflectance profiles: effect of illumination and detection geometry. Opt. Express 29, 15882. https://doi.org/10.1364/oe.421963
Torricelli, A., Spinelli, L., Vanoli, M., Leitner, M., Nemeth, A., Trong, N.N.D., Nicolaï, B., Saeys, W., 2013. 5 - Optical coherence tomography (OCT), space-resolved reflectance spectroscopy (SRS) and time-resolved reflectance spectroscopy (TRS): principles and applications to food microstructures, in: Morris, V.J., Groves, K.B.T.-F.M. (Eds.), Woodhead Publishing Series in Food Science, Technology and Nutrition. Woodhead Publishing, pp. 132–162. https://doi.org/https://doi.org/10.1533/9780857098894.1.132
Tsuchikawa, S., 2002. Application of time-of-flight near-infrared spectroscopy for detecting

water core in apples. J. Am. Soc. Hortic. Sci. 127, 303–308. https://doi.org/10.21273/JASHS.127.2.303

Valero, C., Ruiz-Altisent, M., Cubeddu, R., Pifferi, A., Taroni, P., Torricelli, A., Valentini, G., Johnson, D.S., Dover, C.J., 2004. Detection of internal quality in kiwi with time-domain diffuse reflectance spectroscopy. Appl. Eng. Agric. 20, 223–230. https://doi.org/10.13031/2013.15879

Vanoli, M., Rizzolo, A., Grassi, M., Farina, A., Pifferi, A., Spinelli, L., Torricelli, A., 2011. Time-resolved reflectance spectroscopy nondestructively reveals structural changes in 'Pink Lady®' apples during storage. Procedia Food Sci. 1, 81–89. https://doi.org/10.1016/j.profoo.2011.09.014

Vanoli, M., Van Beers, R., Sadar, N., Rizzolo, A., Buccheri, M., Grassi, M., Lovati, F., Nicolaï, B., Aernouts, B., Watté, R., Torricelli, A., Spinelli, L., Saeys, W., Zanella, A., 2020. Time- and spatially-resolved spectroscopy to determine the bulk optical properties of 'Braeburn' apples after ripening in shelf life. Postharvest Biol. Technol. 168. https://doi.org/10.1016/j.postharvbio.2020.111233

Walsh, K.B., Blasco, J., Zude-Sasse, M., Sun, X., 2020. Visible-NIR 'point' spectroscopy in postharvest fruit and vegetable assessment: The science behind three decades of commercial use. Postharvest Biol. Technol. 168. https://doi.org/10.1016/j.postharvbio.2020.111246

Yang, H.Y., Inagaki, T., Ma, T., Tsuchikawa, S., 2017. High-resolution and non-destructive evaluation of the spatial distribution of nitrate and its dynamics in spinach (Spinacia oleracea l.) leaves by near-infrared hyperspectral imaging. Front. Plant Sci. 8, 1–9. https://doi.org/10.3389/fpls.2017.01937

Zhao, J., Ma, T., Inagaki, T., Chen, Q., Gao, Z., Sun, L., Cai, H., Chen, C., Li, C., Zhang, S., Tsuchikawa, S., Chen, J., 2021. Finite element method simulations and experiments of detachments of lycium barbarum l. Forests 12, 1–12. https://doi.org/10.3390/f12060699

Zhao, J., Sugirbay, A., Chen, Yu, Zhang, S., Liu, F., Bu, L., Chen, Yun, Wang, Z., Chen, J., 2019. FEM explicit dynamics simulation and NIR hyperspectral reflectance imaging for determination of impact bruises of Lycium barbarum L. Postharvest Biol. Technol. 155, 102–110. https://doi.org/10.1016/j.postharvbio.2019.05.024

Zhu, Q., He, C., Lu, R., Mendoza, F., Cen, H., 2015. Ripeness evaluation of "Sun Bright" tomato using optical absorption and scattering properties. Postharvest Biol. Technol. 103, 27–34. https://doi.org/10.1016/j.postharvbio.2015.02.007

Ziosi, V., Noferini, M., Fiori, G., Tadiello, A., Trainotti, L., Casadoro, G., Costa, G., 2008. A new index based on vis spectroscopy to characterize the progression of ripening in peach fruit. Postharvest Biol. Technol. 49, 319–329.

Zude, M., Pflanz, M., Spinelli, L., Dosche, C., Torricelli, A., 2011. Non-destructive analysis of anthocyanins in cherries by means of Lambert-Beer and multivariate regression based on spectroscopy and scatter correction using time-resolved analysis. J. Food Eng. 103, 68–75. https://doi.org/10.1016/j.jfoodeng.2010.09.021